Nano Research 2017, 10(9): 3178–3188
DOI 10.1007/s12274-017-1535-1
Research Article
ISSN 1998-0124
CN 11-5974/O4

Yolk–shell-structured $(Fe_{0.5}Ni_{0.5})_9S_8$ solid-solution powders: Synthesis and application as anode materials for Na-ion batteries

Jung Hyun Kim and Yun Chan Kang (✉)

Department of Materials Science and Engineering, Korea University, Anam-Dong, Seongbuk-Gu, Seoul 136-713, Republic of Korea

Received: 27 November 2016
Revised: 12 February 2017
Accepted: 13 February 2017

KEYWORDS
metal sulfide,
multicomponent sulfide,
yolk–shell,
sodium-ion batteries,
spray pyrolysis

ABSTRACT

Multicomponent metal sulfide materials with a yolk–shell structure and a single phase were studied for the first time as anode materials for sodium-ion batteries. Yolk–shell-structured Fe–Ni–O powders with a molar ratio of iron and nickel components of 1/1 were prepared via one-pot spray pyrolysis. The prepared Fe–Ni–O powders were transformed into yolk–shell-structured $(Fe_{0.5}Ni_{0.5})_9S_8$ solid-solution powders via a sulfidation process. The initial discharge and charge capacities of the $(Fe_{0.5}Ni_{0.5})_9S_8$ powders at a current density of 1 $A{\cdot}g^{-1}$ were 601 and 504 $mA{\cdot}h{\cdot}g^{-1}$, respectively. The discharge capacities of the $(Fe_{0.5}Ni_{0.5})_9S_8$ powders for the 2nd and 100th cycle were 530 and 527 $mA{\cdot}h{\cdot}g^{-1}$, respectively, and their corresponding capacity retention measured from the 2nd cycle was 99%. The $(Fe_{0.5}Ni_{0.5})_9S_8$ powders had high initial discharge and charge capacities at a low current density of 0.1 $A{\cdot}g^{-1}$, and the reversible discharge capacity decreased slightly from 568 to 465 $mA{\cdot}h{\cdot}g^{-1}$ as the current density increased from 0.1 to 5.0 $A{\cdot}g^{-1}$. The synergetic effect of the novel yolk–shell structure and the multicomponent sulfide composition of the $(Fe_{0.5}Ni_{0.5})_9S_8$ powders resulted in excellent sodium-ion storage performance.

1 Introduction

Non-oxide metal compound materials such as sulfides, selenides, tellurides, and phosphides have been studied intensively as anode materials for sodium-ion batteries (SIBs) [1–15]. However, the large volume change and severe pulverization of the active materials during sodiation/desodiation due to the large radius of sodium ions (1.06 Å) limits their application as electrode materials for SIBs [16–19]. In lithium-ion batteries, multicomponent metal compounds have been successfully applied as anode materials [20–23]. These materials can buffer the volume change by separating into single metal compounds during cycling. In addition, the formation of a nanostructure improves the lithium-ion storage performance of multicomponent metal compounds. However, nanostructured non-oxide multiple-metal compound materials have rarely

Address correspondence to yckang@korea.ac.kr

been studied as anode materials for SIBs. Zhao and Manthiram synthesized a $Bi_{0.94}Sb_{1.06}S_3$ solid-solution anode with a nanorod cluster morphology via a hydrothermal reaction [24]. The $Bi_{0.94}Sb_{1.06}S_3$–graphite composite had superior sodium-ion storage performance as compared to Bi_2S_3–graphite and Sb_2S_3–graphite composites. Choi and Kang synthesized yolk–shell SnS–MoS_2 composite microspheres [25]. The synergetic effect of the yolk–shell structure and uniform mixing of the SnS and MoS_2 nanocrystals resulted in excellent sodium-ion storage properties. Spray pyrolysis has many advantages for the preparation of multicomponent materials with yolk–shell structures. Kang et al. synthesized yolk–shell metal oxide powders directly with quinary systems using scalable spray pyrolysis [26]. However, the spray pyrolysis synthesis of multicomponent metal sulfide materials with a yolk–shell structure and a single phase as anode materials for SIBs has not been studied.

In this study, multicomponent metal sulfide materials with a yolk–shell structure and a single phase were studied for the first time as anode materials for SIBs. Yolk–shell-structured Fe–Ni–O powders with a molar ratio of iron and nickel components of 1/1 and multiple phases were prepared via one-pot spray pyrolysis. The prepared Fe–Ni–O powders were transformed into yolk–shell-structured $(Fe_{0.5}Ni_{0.5})_9S_8$ solid-solution powders via a simple post-treatment process. Yolk–shell-structured iron sulfide and nickel sulfide powders and densely structured $(Fe_{0.5}Ni_{0.5})_9S_8$ powders were also prepared by sulfidation of the powders obtained by spray pyrolysis as comparison samples. The electrochemical properties of the prepared samples with various compositions and morphologies for sodium-ion storage were studied to show the synergetic effect of the novel yolk–shell structure and the multicomponent sulfide composition. The results showed the excellent sodium-ion storage performance of the yolk–shell-structured $(Fe_{0.5}Ni_{0.5})_9S_8$ powders.

2 Results and discussion

The formation mechanisms of the yolk–shell-structured Fe–Ni–O and $(Fe_{0.5}Ni_{0.5})_9S_8$ powders are described in Fig. 1. In the first step, i.e., the spray pyrolysis process, the drying of the droplet formed a composite powder (Fig. 1①) consisting of nickel nitrate, iron nitrate, and sucrose. The decomposition of the nickel nitrate and iron nitrate and the carbonization of sucrose formed a NiOx–FeOx–C composite powder (Fig. 1②). The combustion of carbon at the back of the reactor maintained at 700 ˚C produced a carbon-free Fe–Ni–O powder (Fig. 1③) with a mixed crystal structure of $NiFe_2O_4$ and NiO phases [22, 25]. Repetitive combustion and contraction processes produced the multishelled Fe–Ni–O yolk–shell powders. The formation of multishelled metal oxide powders using spray pyrolysis was well described in a previous study [27]. In the second step, i.e., the sulfidation process, the Fe–Ni–O powder was transformed into $(Fe_{0.5}Ni_{0.5})_9S_8$ powder (Fig. 1④). The yolk–shell structure of the oxide powder was maintained even after the sulfidation process.

The morphologies and crystal structures of the Fe–Ni–O powders prepared via the one-pot spray pyrolysis process are shown in Figs. 2 and 3, respectively. The Fe–Ni–O powders had a yolk–shell structure, with a clear void space regardless of the size of the powders, as indicated by the scanning electron microscopy (SEM) and transmission electron microscopy (TEM) images in Figs. 2(a)–2(d). During

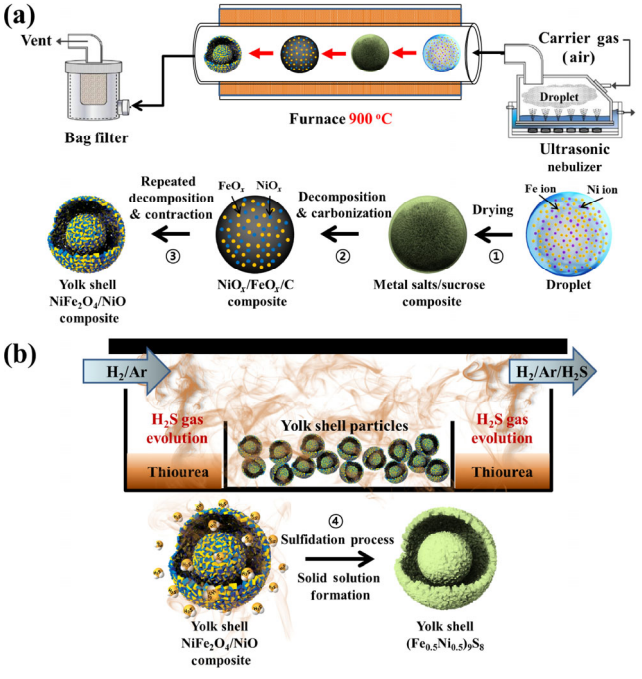

Figure 1 Schematic diagrams of (a) the spray pyrolysis process applied in the preparation of the carbon-free Fe–Ni–O powders with a mixed crystal structure of $NiFe_2O_4$ and NiO phases and (b) the sulfidation process.

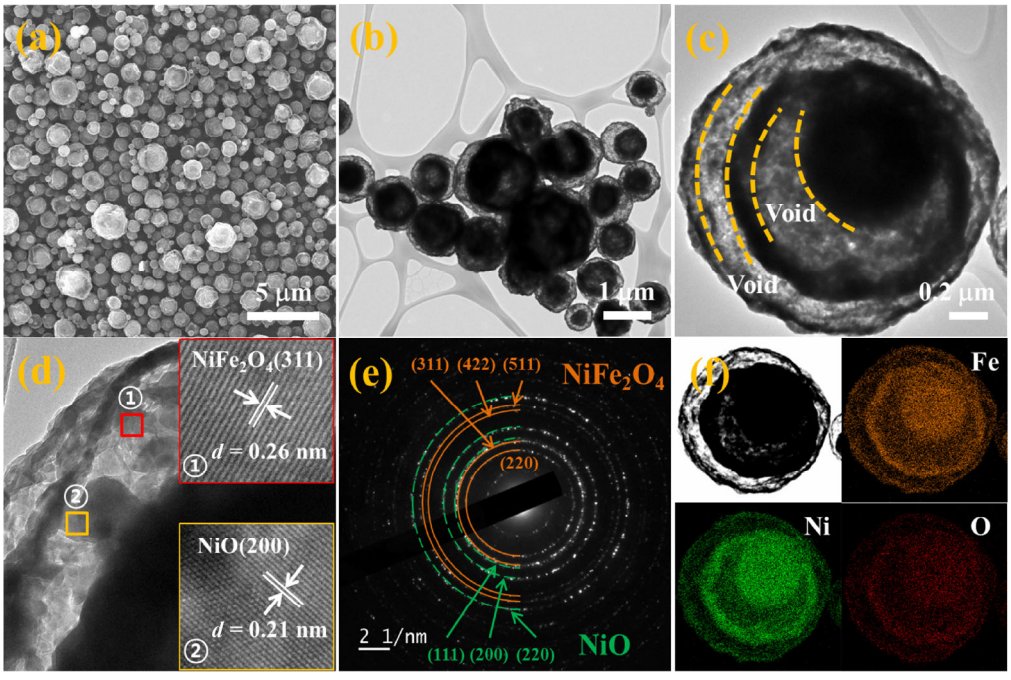

Figure 2 (a) SEM image, (b) and (c) TEM images, (d) high-resolution TEM image, (e) SAED pattern, and (f) elemental mapping images of the Fe–Ni–O yolk–shell powders.

the spray pyrolysis, a yolk–shell powder was formed from one droplet by drying and decomposition inside the tubular reactor. Therefore, the size of the yolk–shell powder depended on the size of the droplet. The Fe–Ni–O powders shown in Fig. 2(c) have clear two shells and one core. The line profile shown in Fig. S1 in the Electronic Supplementary Material (ESM) also revealed the yolk–shell-structured microsphere. The high-resolution TEM image shown in Fig. 2(d) reveals clear lattice fringes separated by 0.26 and 0.21 nm, which correspond to the (311) crystal plane of face-centered cubic (fcc) spinel $NiFe_2O_4$ and the (200) crystal plane of cubic NiO, respectively [28, 29]. The selected-area electron diffraction (SAED) and X-ray diffraction (XRD) patterns shown in Figs. 2(e) and 3 confirm the formation of Fe–Ni–O yolk–shell powders with mixed crystal structures of $NiFe_2O_4$ and NiO. However, the elemental mapping images shown in Fig. 2(f) reveal the uniform distribution of the nickel and iron components throughout the yolk–shell powder. During the spray pyrolysis, the phase separation of the nickel and iron components within the powder was minimized. The Fe–Ni–O yolk–shell-structured microspheres were evaluated by X-ray photoemission spectroscopy (XPS). To understand the bonding environment of the elements, the high-resolution Ni 2p and Fe 2p spectra of the Fe–Ni–O yolk–shell-structured microspheres were analyzed using a Gaussian fitting program, and the results are shown in Figs. S2(a) and S2(b) in the ESM, respectively. As shown in Fig. S2(a) in the ESM, the Ni 2p spectrum consists of two spin-orbit doublets that are characteristic of Ni^{2+}, Ni^{3+}, and two shakeup satellites. The fitting peaks at 854.8 and 872.4 eV are assigned to Ni^{2+}, whereas the fitting peaks at 856.9 and 875.1 eV are assigned to Ni^{3+} [30, 31]. In Fig. S2(b) in the ESM, two main peaks observed at 711.5 and 723.9 eV can be assigned to $Fe2p_{3/2}$ and Fe $2p_{1/2}$, respectively [30]. The Fe $2p_{3/2}$ peak could be best fitted by two components having a minor peak at 710.0 eV and a major peak at 712.6 eV, which could be ascribed to Fe^{2+} and Fe^{3+}, respectively [30]. It is clear that the prepared Fe–Ni–O yolk–shell-structured microspheres contained Ni^{2+} and Fe^{3+}, which are characteristic of $NiFe_2O_4$ and NiO phases.

The XRD pattern of the powders obtained after the sulfidation of the Fe–Ni–O yolk–shell powders is shown in Fig. 3. Single-phase pentlandite $(Fe_{0.5}Ni_{0.5})_9S_8$ powders without an impurity phase were prepared by simple sulfidation at 300 °C.

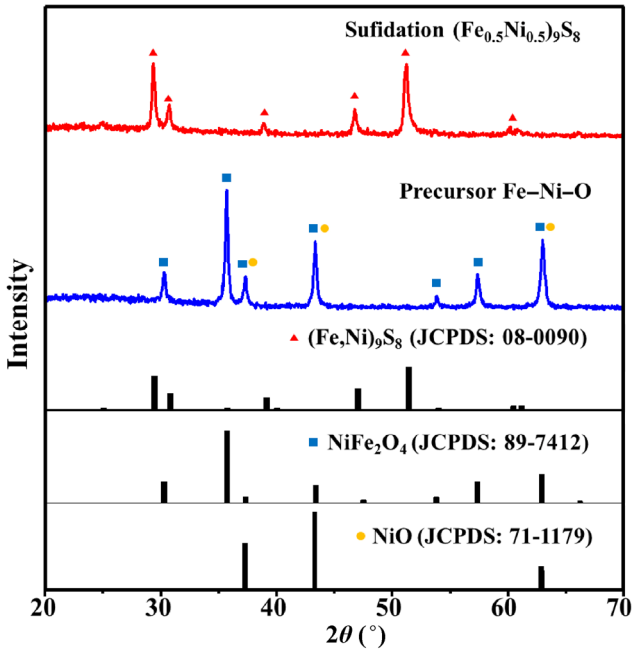

Figure 3 XRD patterns of the Fe–Ni–O and $(Fe_{0.5}Ni_{0.5})_9S_8$ yolk–shell powders obtained before and after the sulfidation process.

The pentlandite $(Fe_{0.5}Ni_{0.5})_9S_8$ powders had a clear yolk–shell structure, as confirmed by the SEM and TEM images shown in Figs. 4(a)–4(c). Ultrafine nanocrystals less than 50 nm in size comprised the shell part, as indicated by the TEM image shown in Fig. 4(c). The high-resolution TEM image shown in Fig. 4(d) reveals clear lattice fringes separated by 0.30 nm, which correspond to the (311) crystal plane of the pentlandite $(Fe_{0.5}Ni_{0.5})_9S_8$ powder. The SAED pattern and elemental mapping images shown in Figs. 4(e) and 4(f), respectively, confirm the formation of a highly uniform $(Fe_{0.5}Ni_{0.5})_9S_8$ powder without an impurity phase and with compositional homogeneity.

The chemical state and molecular environment of the $(Fe_{0.5}Ni_{0.5})_9S_8$ yolk–shell powders were characterized by XPS, as shown in Fig. 5. The XPS survey spectrum in Fig. 5(a) confirms the presence of Ni, Fe, O, and S signals. In the Fe 2p spectrum of the powders, which is shown in Fig. 5(b), small peaks arose at binding energies of 710.1 eV for Fe $2p_{3/2}$ and 723.6 eV for Fe $2p_{1/2}$, which are ascribed to the Fe^{2+} states in the Fe 2p spectrum of the FeS phase [32, 33]. The peaks with a higher binding energy located at 712.5 eV for Fe $2p_{3/2}$ and 725.8 eV for Fe $2p_{1/2}$ can be assigned to oxide-related Fe^{3+} ions, which is characteristic of iron oxide (Fe_3O_4) [32]. The $(Fe_{0.5}Ni_{0.5})_9S_8$ surface was converted with iron oxide (Fe_3O_4) because of the high reactivity of metal sulfide with oxygen. In the Ni 2p spectrum (Fig. 5(c)), the major peak at 855.3 eV and its associated satellite (861.0 eV) are those of Ni^{2+} bonded to sulfur [34–36]. The binding energies at 852.6 and 870.0 eV can

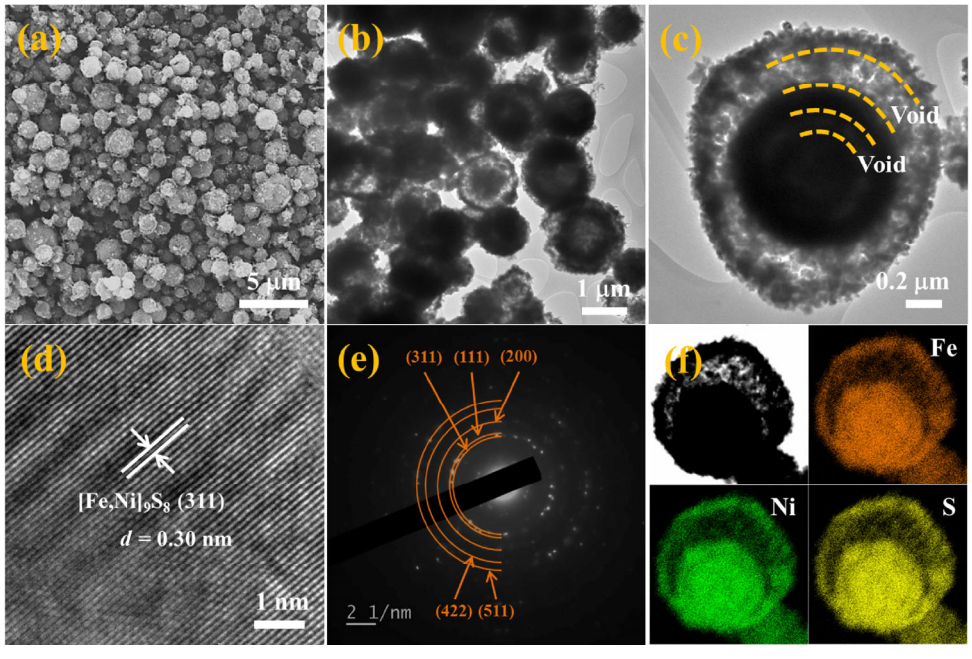

Figure 4 (a) SEM image, (b) and (c) TEM images, (d) high-resolution TEM image, (e) SAED pattern, and (f) elemental mapping images of the $(Fe_{0.5}Ni_{0.5})_9S_8$ yolk–shell powders.

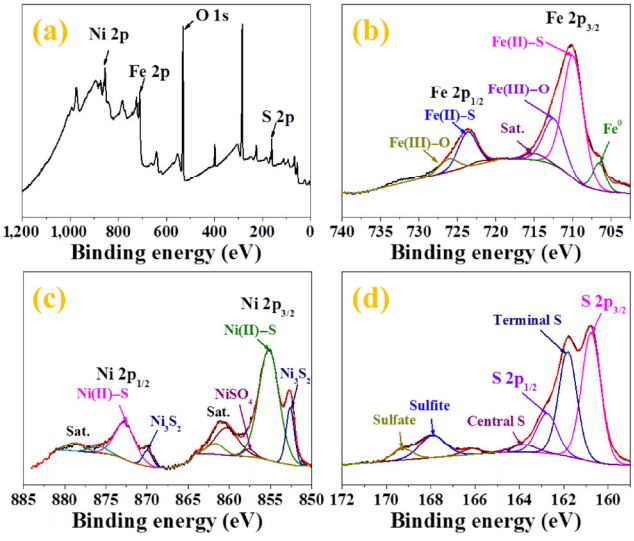

Figure 5 XPS spectra of the $(Fe_{0.5}Ni_{0.5})_9S_8$ yolk–shell powders: (a) survey scan, (b) Fe 2p, (c) Ni 2p, and (d) S 2p.

be assigned to the characteristic peaks of Ni_3S_2 [36]. The other peak at 857.7 eV implies the presence of $NiSO_4$ [35]. There is clear evidence for SO_4^{2-} in the S 2p spectrum shown in Fig. 5(d). The oxidation peak is intense in the nickel and iron signals, which is ascribed to both adsorbed contamination and the presence of sulfates as oxidation products. This is confirmed by the signal of the sulfur S 2p high-resolution spectrum at binding energy values higher than 167 eV. Polysulfides are chains of sulfur atoms of varying lengths. The sulfur atoms in the center of the chain can be distinguished from those at the end of the chain. In the S 2p spectrum, 161.7 and 163.7 eV are assigned to terminal sulfur and central sulfur, respectively [37]. The core-level band of the S 2p region is observed, and the peaks at 160.7 and 162.7 eV correspond to S $2p_{3/2}$ and S $2p_{1/2}$, respectively, which are characteristic of sulfide [37].

The electrochemical properties of the yolk–shell-structured Fe–Ni–O and $(Fe_{0.5}Ni_{0.5})_9S_8$ powders for sodium-ion storage were investigated via cyclic voltammetry (CV) and galvanostaticcharge/discharge tests in the potential range of 0.01–3 V vs. Na/Na^+. The cyclic voltammograms of the $(Fe_{0.5}Ni_{0.5})_9S_8$ and Fe–Ni–O powders during the first five cycles at a scan rate of 0.1 $mV{\cdot}s^{-1}$ are shown in Figs. 6(a) and 6(b), respectively. The first cathodic scan of the $(Fe_{0.5}Ni_{0.5})_9S_8$ powders shows one sharp peak and one small reduction peak at 0.67 and 0.32 V, respectively. The sharp reduction peak at 0.67 V with the largest current intensity is attributed to the following reaction: $(Fe_{0.5}Ni_{0.5})_9S_8 + 16Na^+ + 16e^- \rightarrow 4.5Fe + 4.5Ni + 8Na_2S$ [38, 39]. The small peak at 0.32 V is attributed to the decomposition of the electrolyte and the formation of a solid electrolyte interface layer on the surface of the $(Fe_{0.5}Ni_{0.5})_9S_8$ electrode [38, 39]. The broad oxidation peaks observed between 1.1 and 2.2 V in the anodic scans of the $(Fe_{0.5}Ni_{0.5})_9S_8$ powders are mainly attributed to the formation of NiS_x and FeS_x from metallic nickel and iron nanocrystals and Na_2S [38–41]. The formation of ultrafine NiS and FeS nanocrystals during the first cycle resulted in the reduction peak shifting to a high potential from the second cycle onward, as shown in Fig. 6(a) [42]. The morphologies and SAED pattern of the yolk–shell $(Fe_{0.5}Ni_{0.5})_9S_8$ powders obtained after the first discharge and charge processes are shown in Figs. S3 and S4 in the ESM, respectively. The ultrafine metallic Ni and Fe nanocrystals were formed during the first discharge process, as confirmed by the TEM images and SAED pattern shown in Fig. S3 in the ESM. The Ni and Fe nanocrystals transformed into the ultrafine NiS and FeS nanocrystals after the first charge process, as shown in Fig. S4 in the ESM. The $(Fe_{0.5}Ni_{0.5})_9S_8$ nanocrystals, which are several tens of nanometers in size, transformed into the ultrafine NiS and FeS nanocrystals after the first discharge and charge processes, as confirmed by the TEM images and SAED pattern. After the first cycle, the reduction and oxidation peaks in the CV tests overlapped substantially, indicating the stable performance of the $(Fe_{0.5}Ni_{0.5})_9S_8$ powders under repeated Na^+ insertion and extraction. However, the Fe–Ni–O yolk–shell powders did not exhibit distinct reduction and oxidation peaks in the CV curves, as shown in Fig. 6(b). The XRD patterns of the yolk–shell-structured Fe–Ni–O powders obtained after the first discharge and charge processes are shown in Fig. S5 in the ESM. $NiFe_2O_4$ and NiO crystal phases were observed even after the first discharge and charge processes. The result revealed the poor sodium-ion storage performance of the Fe–Ni–O powders. The initial discharge and charge curves of the $(Fe_{0.5}Ni_{0.5})_9S_8$ powders at a current density of 1 $A{\cdot}g^{-1}$ are shown in Fig. 6(c). A clear plateau around 0.67 V is observed in the initial discharge curve of the $(Fe_{0.5}Ni_{0.5})_9S_8$ powders, which was due to the formation of Ni, Fe, and Na_2S [38, 39]. However,

the initial discharge curve of the Fe–Ni–O powders did not show a plateau. The results of the initial discharge and charge curves of the two samples agree well with those of the CV curves. A sufficient conversion reaction of the Fe–Ni–O powders with Na^+ did not occur during the discharge process. The initial discharge and charge capacities of the $(Fe_{0.5}Ni_{0.5})_9S_8$ powders were 601 and 504 mA·h·g^{-1}, respectively, and their corresponding initial coulombic efficiency was 84%. The discharge capacities of the $(Fe_{0.5}Ni_{0.5})_9S_8$ powders for the 2nd and 100th cycles at a current density of 1 A·g^{-1} were 530 and 527 mA·h·g^{-1}, respectively, as shown in Fig. 6(d), and their corresponding capacity retention measured from the 2nd cycle was 99%. The discharge capacities of the $(Fe_{0.5}Ni_{0.5})_9S_8$ powders remained constant during the first 30 cycles and then slightly increased with increasing cycle number. The reason for the capacity increase of the $(Fe_{0.5}Ni_{0.5})_9S_8$ powders during the cycling is explained by the following impedance spectra. The rate performances of the Fe–Ni–O and $(Fe_{0.5}Ni_{0.5})_9S_8$ powders are shown in Fig. 6(e), where the current density increases stepwise from 0.1 to 5 A·g^{-1} and then decreases to 0.1 A·g^{-1}. The $(Fe_{0.5}Ni_{0.5})_9S_8$ powders had high initial discharge and charge capacities at a low current density of 0.1 A·g^{-1}, and the reversible discharge capacities decreased slightly from 568 to 465 mA·h·g^{-1} as the current density increased from 0.1 to 5.0 A·g^{-1}. The discharge capacity of the $(Fe_{0.5}Ni_{0.5})_9S_8$ powders well recovered when the current density was returned into 0.1 A·g^{-1} after cycling at high current densities. However, the Fe–Ni–O powders had extremely low discharge and charge capacities even at a low current density of 0.1 A·g^{-1}.

The electrochemical impedance spectra of the Fe–Ni–O and $(Fe_{0.5}Ni_{0.5})_9S_8$ powders obtained before and after 1, 10, 50, 80, and 100 cycles are shown in Fig. 7. The Nyquist plots indicate compressed semicircles in the medium-frequency range of each spectrum, which describe the charge-transfer resistance (R_{ct}) for both electrodes [43, 44]. Before cycling, the two yolk–shell-structured powders had similar charge-transfer resistances of ~700 Ω. Generally, metal sulfide materials

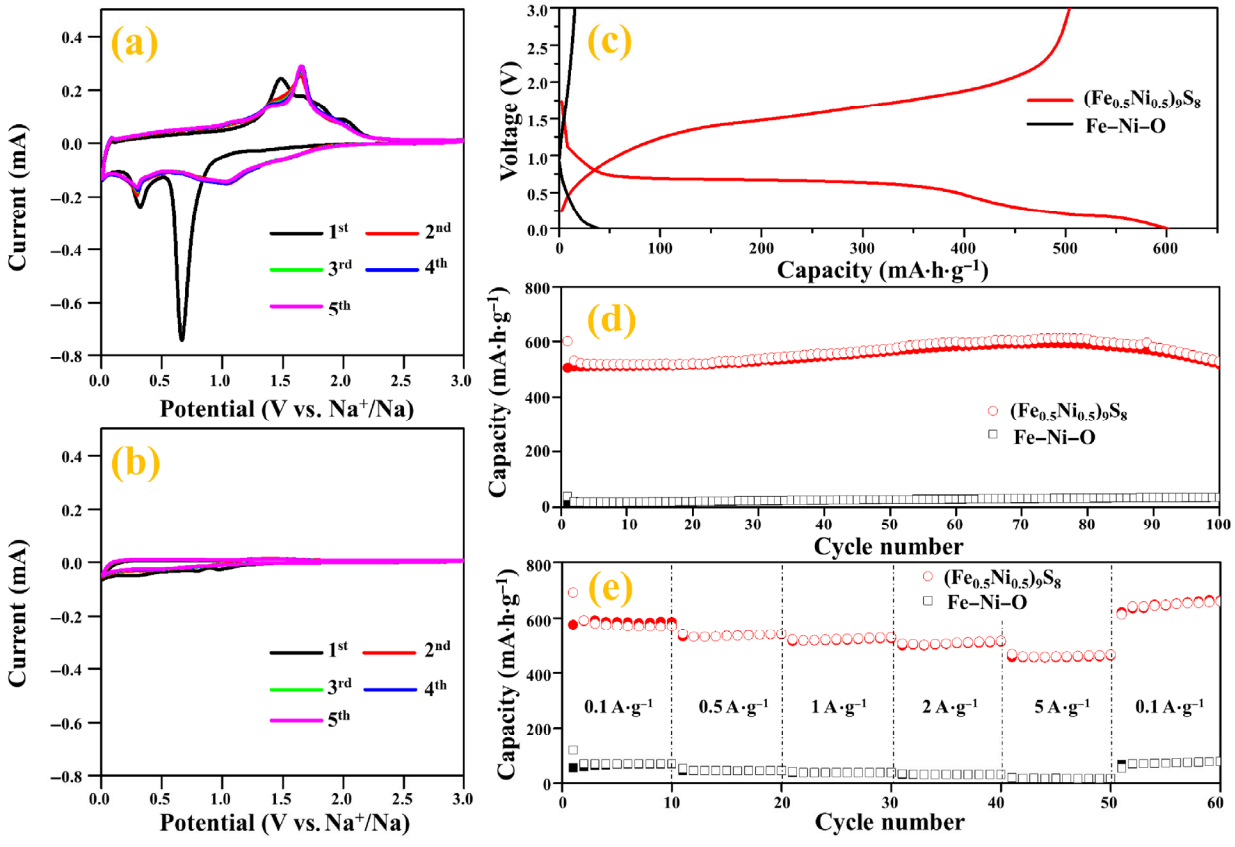

Figure 6 Electrochemical properties of the Fe–Ni–O and $(Fe_{0.5}Ni_{0.5})_9S_8$ yolk–shell powders: (a) CV curves of $(Fe_{0.5}Ni_{0.5})_9S_8$, (b) CV curves of Fe–Ni–O, (c) initial discharge and charge curves, (d) cycling performance, and (e) rate performance.

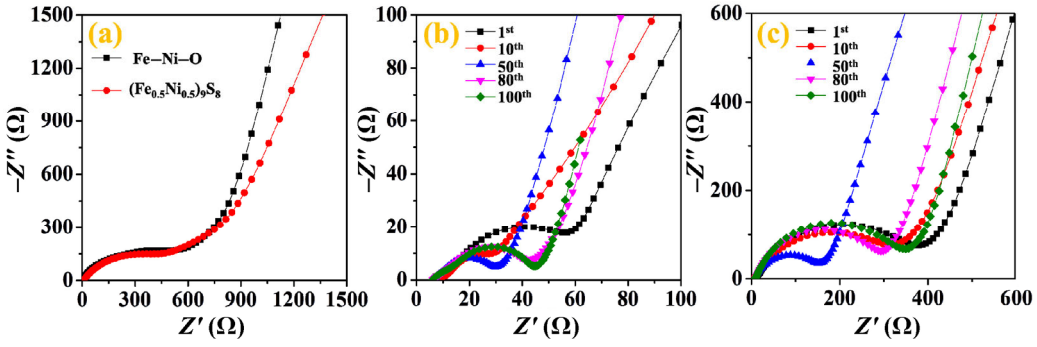

Figure 7 Nyquist plots of the Fe–Ni–O and $(Fe_{0.5}Ni_{0.5})_9S_8$ yolk–shell powders (a) before cycling, (b) after cycling of $(Fe_{0.5}Ni_{0.5})_9S_8$, and (c) after cycling of Fe–Ni–O.

have higher electrical conductivities than oxide materials. In this study, the sulfidation process decreased the surface area of the yolk–shell-structured powders. Therefore, the contact area of the powders with the liquid electrolyte decreased after the sulfidation process. The two compensating effects resulted in similar charge-transfer resistances for the two samples before cycling. The charge-transfer resistance of the $(Fe_{0.5}Ni_{0.5})_9S_8$ powders decreased to 55 Ω after the first cycle because of the formation of ultrafine nanocrystals during the first discharge and charge processes. The further decrease of the charge-transfer resistance after 50 cycles revealed the stepwise activation of the $(Fe_{0.5}Ni_{0.5})_9S_8$ powders over the 50 cycles. Therefore, the discharge capacities of the yolk–shell-structured $(Fe_{0.5}Ni_{0.5})_9S_8$ powders continuously increased as a function of the cycle number from the 2nd cycle onward, as shown in Fig. 6(d). However, capacity fading due to the partial structural damage of the yolk–shell-structured $(Fe_{0.5}Ni_{0.5})_9S_8$ powders offset the capacity increase due to stepwise activation during the cycling. The charge-transfer resistance of the $(Fe_{0.5}Ni_{0.5})_9S_8$ powders increased to 42 Ω after the 80th cycle and it remained constant over an additional 20 cycles, as shown in Fig. 7(b). Therefore, the $(Fe_{0.5}Ni_{0.5})_9S_8$ powders had good cycling performance during the 100 cycles, as shown in Fig. 6(d). Slow and stepwise activation occurred in the yolk–shell-structured Fe–Ni–O powders, as confirmed by the Nyquist plots shown in Fig. 7(c). The charge-transfer resistance decreased from 722 to 156 Ω during the first 50 cycles. However, the structural destruction of the Fe–Ni–O powders during repeated sodium-ion insertion and extraction processes increased the charge-transfer resistance to 364 Ω after the 100th cycle.

The electrochemical properties of the yolk–shell-structured $(Fe_{0.5}Ni_{0.5})_9S_8$ powders were also compared to those of single- and multi-component sulfide powders with dense structures (denoted as Fe–S@D, Ni–S@D, and Fe–Ni–S@D) and single-component sulfide powders with a yolk–shell structure (denoted as Fe–S@Y and Ni–S@Y). Metal sulfide powders with dense structures were prepared by sulfidation of the metal oxide powders with dense structures, which were prepared from the spray solution without sucrose. The yolk–shell-structured Fe–S@Y and Ni–S@Y powders were prepared by sulfidation of the Fe–O@Y and Ni–O@Y powders with yolk–shell structures obtained by spray pyrolysis. The morphologies of the metal sulfide powders with dense and yolk–shell structures are shown in Fig. S6 in the ESM. The initial discharge and charge curves and cycling performance of powders with different compositions and morphologies at a current density of 1 $A \cdot g^{-1}$ are shown in Fig. S7 in the ESM. The initial discharge capacities of the Fe–S@D, Ni–S@D, and Fe–Ni–S@D powders were 375, 467, and 458 $mA \cdot h \cdot g^{-1}$, respectively, and their discharge capacities for the 80th cycle were 351, 293, and 439 $mA \cdot h \cdot g^{-1}$, respectively. However, the initial discharge capacities of the Fe–S@Y, Ni–S@Y, and Fe–Ni–S@Y powders were 426, 563, and 601 $mA \cdot h \cdot g^{-1}$, respectively, and their discharge capacities for the 80th cycle were 351, 293, and 439 $mA \cdot h \cdot g^{-1}$, respectively. The multicomponent metal sulfide powders had higher discharge capacities

than the single-component metal sulfide powders, irrespective of their morphologies. In addition, the yolk–shell-structured metal sulfide powders had superior sodium-ion storage performance as compared to the dense-structured powders with the same composition. The morphologies of the $(Fe_{0.5}Ni_{0.5})_9S_8$ powders with dense and yolk–shell structures obtained after 50 cycles are shown in Fig. S8 in the ESM. The spherical morphology of the yolk–shell powders was completely maintained even after cycling as shown in Fig. S8(a) in the ESM. On the other hand, the spherical morphology of the powders with a dense structure was destroyed after cycling, as shown in Fig. S8(b) in the ESM. The yolk–shell-structured $(Fe_{0.5}Ni_{0.5})_9S_8$ powders with high structural stability during cycling exhibited good characteristics as anode materials for SIBs. The synergetic effect of the novel yolk–shell structure and multicomponent sulfide composition resulted in the excellent sodium-ion storage performance of the yolk–shell-structured $(Fe_{0.5}Ni_{0.5})_9S_8$ powders.

The sodium-ion storage performance of the current yolk–shell-structured $(Fe_{0.5}Ni_{0.5})_9S_8$ powders was compared to that of chalcogenide materials with various morphologies reported in previous studies, and the results are summarized in Table S1 in the ESM. The yolk–shell-structured $(Fe_{0.5}Ni_{0.5})_9S_8$ powders with high electrical conductivity and unique morphology showed superior sodium-ion storage performance at high current densities as compared to that of chalcogenide materials with various morphologies.

3 Conclusions

Multicomponent metal sulfide solid-solution powders were prepared for the first time by applying a spray pyrolysis process and a subsequent single-step sulfidation process. The yolk–shell structure of the Fe–Ni–O powders prepared by spray pyrolysis was well maintained even after complete sulfidation for $(Fe_{0.5}Ni_{0.5})_9S_8$ solid-solution powders. Electrochemical impedance spectroscopy and galvanostatic charge/discharge tests revealed the stepwise activation of the $(Fe_{0.5}Ni_{0.5})_9S_8$ powders with high crystallinity over 50 cycles at a high current density of 1 $A{\cdot}g^{-1}$. The yolk–shell-structured $(Fe_{0.5}Ni_{0.5})_9S_8$ powders exhibited superior sodium-ion storage performance as compared to the Fe–Ni–O powders with a similar morphology. However, the yolk–shell-structured $(Fe_{0.5}Ni_{0.5})_9S_8$ powders did not show excellent cycling stability during long-term cycling over 100 cycles. The structural stability of the multicomponent metal sulfide solid-solution powders with a yolk–shell structure should be further improved in terms of repetitive Na^+ insertion and extraction processes by applying carbon materials for application as anode materials for SIBs. The strategy employed in this study can be applied in multicomponent yolk–shell-structured metal sulfide powders for a wide range of applications, including energy storage.

4 Experimental

$(Fe_{0.5}Ni_{0.5})_9S_8$ solid-solution powders were prepared by spray pyrolysis and subsequent sulfidation. Yolk–shell-structured Fe–Ni–O powders with a molar ratio of iron and nickel components of 1/1 were prepared via one-pot spray pyrolysis using a spray solution with sucrose as the carbon source. The preparation of the yolk–shell metal oxide powders via spray pyrolysis and sulfidation is described in our previous article [25]. During the spray-pyrolysis process, the reactor temperature was maintained at 700 °C. Air was used as the carrier gas at a flow rate of 5 $L{\cdot}min^{-1}$. The aqueous spray solution was prepared using nickel nitrate hexahydrate $[Ni(NO_3)_2{\cdot}6H_2O]$, iron nitrate nonahydrate $[Fe(NO_3)_3{\cdot}9H_2O]$, and sucrose ($C_{12}H_{22}O_{11}$). The total concentration of the nickel and iron components dissolved in distilled water was 0.5 M. The concentration of sucrose used as the carbon source was fixed at 0.5 M. The sulfidation process was conducted at 300 °C for 6 h in H_2S gas, which was formed from commercial thiourea powders by hydrogen gas. For the sulfidation process, the Fe–Ni–O powders and thiourea powders were loaded into a covered alumina boat and placed in a quartz-tube reactor.

The crystal structures of the two yolk–shell-structured samples were investigated using XRD (X'Pert PRO MPD) with Cu Kα radiation (λ = 1.5418 Å) at the Korea Basic Science Institute (Daegu). XPS (Thermo Scientific K-Alpha) with focused monochromatic Al Kα at 12 kV

and 20 mA was used to analyze the compositions of the specimens. The morphologies of the nanofibers were characterized using SEM (TESCAN VEGA3-SB) and field-emission TEM (JEOL, JEM-2100F) at a working voltage of 200 kV.

The electrochemical properties of the two yolk–shell-structured samples were analyzed by constructing a 2032-type coin cell. The anode was prepared by mixing the active material, carbon black, and sodium carboxymethyl cellulose at a weight ratio of 7:2:1. Sodium metal and a microporous polypropylene film were used as the counter electrode and the separator, respectively. The electrolyte was 1 M $NaClO_4$ (Aldrich) dissolved in a mixture of ethylene carbonate and dimethyl carbonate (EC/DMC, 1/1 v/v), to which 5 wt.% fluoroethylene carbonate was added. The discharge–charge characteristics of the samples were investigated by cycling the cells in a 0.01–3 V potential range at various current densities. Cyclic voltammograms were measured at a scan rate of 0.1 $mV \cdot s^{-1}$. The dimensions of the anode were 1 cm × 1 cm, and the mass loading was ~1.2 $mg \cdot cm^{-2}$. The electrochemical impedance spectra of the nanofibers were obtained over the 0.01 Hz to 100 kHz frequency range at room temperature with a signal amplitude of 5 mV.

Acknowledgements

This work was supported by a National Research Foundation of Republic of Korea (NRF) grant funded by the Korea government (MEST) (No. NRF-2015R1A2A1A15056049).

Electronic Supplementary Material: Supplementary material (morphologies and phase analysis of the Fe–Ni–O yolk–shell powders, morphologies of the Fe–Ni–O, $(Fe_{0.5}Ni_{0.5})_9S_8$ yolk–shell powders obtained after the first charge and discharge, morphologies, XRD patterns and electrochemical properties of the Fe–S@D, Ni–S@D, Fe–Ni–S@D, Fe–S@Y and Ni–S@Y powders, morphology of the powders obtained after cycling, XRD patterns, morphologies and rate performances of the $(Fe_{0.5}Ni_{0.5})_9S_8$ yolk–shell powders obtained at various sulfidation temperatures) is available in the online version of this article at https://doi.org/10.1007/s12274-017-1535-1.

References

[1] Kim, Y.; Kim, Y.; Choi, A.; Woo, S.; Mok, D.; Choi, N. S.; Jung, Y. S.; Ryu, J. H.; Oh, S. M.; Lee, K. T. Tin phosphide as a promising anode material for Na-ion batteries. *Adv. Mater.* **2014**, *26*, 4139–4144.

[2] Jang, J. Y.; Lee, Y.; Kim, Y.; Lee, J.; Lee, S. M.; Lee, K. T.; Choi, N. S. Interfacial architectures based on a binary additive combination for high-performance Sn_4P_3 anodes in sodium-ion batteries. *J. Mater. Chem. A* **2015**, *3*, 8332–8338.

[3] Choi, S. H.; Ko, Y. N.; Lee, J. K.; Kang, Y. C. 3D MoS_2-graphene microspheres consisting of multiple nanospheres with superior sodium ion storage properties. *Adv. Funct. Mater.* **2015**, *25*, 1780–1788.

[4] Xu, X. J.; Ji, S. M.; Gu, M. Z.; Liu, J. *In situ* synthesis of MnS hollow microspheres on reduced graphene oxide sheets as high-capacity and long-life anodes for Li- and Na-ion batteries. *ACS Appl. Mater. Interfaces* **2015**, *7*, 20957–20964.

[5] Hu, Z.; Zhu, Z. Q.; Cheng, F. Y.; Zhang, K.; Wang, J. B.; Chen, C. C.; Chen, J. Pyrite FeS_2 for high-rate and long-life rechargeable sodium batteries. *Energy Environ. Sci.* **2015**, *8*, 1309–1316.

[6] You, Y.; Yu, X. Q.; Yin, Y. X.; Nam, K. W.; Guo, Y. G. Sodium iron hexacyanoferrate with high Na content as a Na-rich cathode material for Na-ion batteries. *Nano Res.* **2015**, *8*, 117–128.

[7] Zhang, Z. A.; Shi, X. D.; Yang, X.; Fu, Y.; Zhang, K.; Lai, Y. Q.; Li, J. Nanooctahedra particles assembled $FeSe_2$ microspheres embedded into sulfur-doped reduced graphene oxide sheets as a promising anode for sodium ion batteries. *ACS Appl. Mater. Interfaces* **2016**, *8*, 13849–13856.

[8] Park, J.; Kim, J. S.; Park, J. W.; Nam, T. H.; Kim, K. W.; Ahn, J. H.; Wang, G. X.; Ahn, H. J. Discharge mechanism of MoS_2 for sodium ion battery: Electrochemical measurements and characterization. *Electrochim. Acta* **2013**, *92*, 427–432.

[9] Ko, Y. N.; Choi, S. H.; Kang, Y. C. Hollow cobalt selenide microspheres: Synthesis and application as anode materials for Na-ion batteries. *ACS Appl. Mater. Interfaces* **2016**, *8*, 6449–6456.

[10] Kim, T. B.; Choi, J. W.; Ryu, H. S.; Cho, G. B.; Kim, K. W.; Ahn, J. H.; Cho, K. K.; Ahn, H. J. Electrochemical properties of sodium/pyrite battery at room temperature. *J. Power Sources* **2007**, *174*, 1275–1278.

[11] Saha, P.; Jampani, P. H.; Datta, M. K.; Hong, D.; Okoli, C. U.; Manivannan, A.; Kumta, P. N. Electrochemical performance of chemically and solid state-derived chevrel phase Mo_6T_8 (T = S, Se) positive electrodes for sodium-ion batteries. *J. Phys. Chem. C* **2015**, *119*, 5771–5782.

[12] Zhang, K.; Hu, Z.; Liu, X.; Tao, Z. L.; Chen, J. $FeSe_2$ microspheres as a high-performance anode material for Na-ion batteries. *Adv. Mater.* **2015**, *27*, 3305–3309.

[13] Yu, D. Y. W.; Prikhodchenko, P. V.; Mason, C. W.; Batabyal, S. K.; Gun, J.; Sladkevich, S.; Medvedev, A. G.; Lev, O. High-capacity antimony sulphide nanoparticle-decorated graphene composite as anode for sodium-ion batteries. *Nat. Commun*. **2013**, *4*, 2922.

[14] Kim, Y.; Kim, Y.; Park, Y.; Jo, Y. N.; Kim, Y. J.; Choi, N. S.; Lee, K. T. SnSe alloy as a promising anode material for Na-ion batteries. *Chem. Commun*. **2015**, *51*, 50–53.

[15] Cho, J. S.; Lee, S. Y.; Lee, J. K.; Kang, Y. C. Iron telluride-decorated reduced graphene oxide hybrid microspheres as anode materials with improved Na-ion storage properties. *ACS Appl. Mater. Interfaces* **2016**, *8*, 21343–21349.

[16] Ong, S. P.; Chevrier, V. L.; Hautier, G.; Jain, A.; Moore, C.; Kim, S.; Ma, X. H.; Ceder, G. Voltage, stability and diffusion barrier differences between sodium-ion and lithium-ion intercalation materials. *Energy Environ. Sci*. **2011**, *4*, 3680–3688.

[17] Klein, F.; Jache, B.; Bhide, A.; Adelhelm, P. Conversion reactions for sodium-ion batteries. *Phys. Chem. Chem. Phys.* **2013**, *15*, 15876–15887.

[18] Xu, Y. H.; Zhu, Y. J.; Liu, Y. H.; Wang, C. S. Electrochemical performance of porous carbon/tin composite anodes for sodium-ion and lithium-ion batteries. *Adv. Energy Mater.* **2013**, *3*, 128–133.

[19] Ellis, B. L.; Nazar, L. F. Sodium and sodium-ion energy storage batteries. *Curr. Opin. Solid State Mater. Sci.* **2012**, *16*, 168–177.

[20] Sharma, Y.; Sharma, N.; Rao, G. V. S.; Chowdari, B. V. R. Nanophase $ZnCo_2O_4$ as a high performance anode material for Li-ion batteries. *Adv. Funct. Mater.* **2007**, *17*, 2855–2861.

[21] Choi, S. H.; Kang, Y. C. Synergetic compositional and morphological effects for improved Na^+ storage properties of $Ni_3Co_6S_8$-reduced graphene oxide composite powders. *Nanoscale* **2015**, *7*, 6230–6237.

[22] Choi, S. H.; Kang, Y. C. Using simple spray pyrolysis to prepare yolk–shell-structured ZnO–Mn_3O_4 systems with the optimum composition for superior electrochemical properties. *Chem.—Eur. J.* **2014**, *20*, 3014–3018.

[23] Park, K.-S.; Seo, S.-D.; Shim, H.-W.; Kim, D.-W. Electrochemical performance of $Ni_xCo_{1-x}MoO_4$ ($0 \le x \le 1$) nanowire anodes for lithium-ion batteries. *Nanoscale Res. Lett.* **2012**, *7*, 35.

[24] Zhao, Y. B.; Manthiram, A. $Bi_{0.94}Sb_{1.06}S_3$ nanorod cluster anodes for sodium-ion batteries: Enhanced reversibility by the synergistic effect of the Bi_2S_3-Sb_2S_3 solid solution. *Chem. Mater.* **2015**, *27*, 6139–6145.

[25] Choi, S. H.; Kang, Y. C. Synergetic effect of yolk–shell structure and uniform mixing of SnS-MoS_2 nanocrystals for improved Na-ion storage capabilities. *ACS Appl. Mater. Interfaces* **2015**, *7*, 24694–24702.

[26] Hong, Y. J.; Son, M. Y.; Park, B. K.; Kang, Y. C. One-pot synthesis of yolk–shell materials with single, binary, ternary, quaternary, and quinary systems. *Small* **2013**, *9*, 2224–2227.

[27] Hong, Y. J.; Son, M. Y.; Kang, Y. C. One-pot facile synthesis of double-shelled SnO_2 yolk–shell-structured powders by continuous process as anode materials for Li-ion batteries. *Adv. Mater.* **2013**, *25*, 2279–2283.

[28] Qu, S.; Wang, J.; Kong, J. L.; Yang, P. Y.; Chen, G. Magnetic loading of carbon nanotube/nano-Fe_3O_4 composite for electrochemical sensing. *Talanta* **2007**, *71*, 1096–1102.

[29] Wang, C.; Wang, T. S.; Wang, B. Q.; Zhou, X.; Cheng, X. Y.; Sun, P.; Zheng, J.; Lu, G. Y. Design of α-Fe_2O_3 nanorods functionalized tubular NiO nanostructure for discriminating toluene molecules. *Sci. Rep.* **2016**, *6*, 26432.

[30] Uddin, M. E.; Kim, N. H.; Kuila, T.; Lee, S. H.; Hui, D.; Lee, J. H. Preparation of reduced graphene oxide-$NiFe_2O_4$ nanocomposites for the electrocatalytic oxidation of hydrazine. *Compos. Part B-Eng.* **2015**, *79*, 649–659.

[31] Liu, X. J.; Liu, J. F.; Sun, X. M. $NiCo_2O_4$@NiO hybrid arrays with improved electrochemical performance for pseudocapacitors. *J. Mater. Chem. A* **2015**, *3*, 13900–13905.

[32] Seefeld, S.; Limpinsel, M.; Liu, Y.; Farhi, N.; Weber, A.; Zhang, Y. N.; Berry, N.; Kwon, Y. J.; Perkins, C. L.; Hemminger, J. C. et al. Iron pyrite thin films synthesized from an $Fe(acac)_3$ ink. *J. Am. Chem. Soc.* **2013**, *135*, 4412–4424.

[33] Park, B. I.; Yu, S.; Hwang, Y.; Cho, S. H.; Lee, J. S.; Park, C.; Lee, D. K.; Lee, S. Y. Highly crystalline Fe_2GeS_4 nanocrystals: Green synthesis and their structural and optical characterization. *J. Mater. Chem. A* **2015**, *3*, 2265–2270.

[34] Legrand, D. L.; Nesbitt, H. W.; Bancroft, G. M. X-ray photoelectron spectroscopic study of a pristine millerite (NiS) surface and the effect of air and water oxidation. *Am. Mineral.* **1998**, *83*, 1256–1265.

[35] Jiang, N.; Bogoev, L.; Popova, M.; Gul, S.; Yano, J.; Sun, Y. J. Electrodeposited nickel-sulfide films as competent hydrogen evolution catalysts in neutral water. *J. Mater. Chem. A* **2014**, *2*, 19407–19414.

[36] Wang, X. B.; Hao, J.; Su, Y. C.; Liu, F. G.; An, J.; Lian, J. S. A $Ni_{1-x}Zn_xS$/Ni foam composite electrode with multi-layers: One-step synthesis and high supercapacitor performance. *J. Mater. Chem. A* **2016**, *4*, 12929–12939.

[37] Fantauzzi, M.; Elsener, B.; Atzei, D.; Rigoldi, A.; Rossi, A. Exploiting XPS for the identification of sulfides and polysulfides. *RSC Adv.* **2015**, *5*, 75953–75963.

[38] Wang, Y. X.; Yang, J. P.; Chou, S. L.; Liu, H. K.; Zhang, W. X.; Zhao, D. Y.; Dou, S. X. Uniform yolk–shell iron sulfide-carbon nanospheres for superior sodium-iron sulfide batteries. *Nat. Commun.* **2015**, *6*, 8689.

[39] Kang, H. Y.; Liu, Y. C.; Cao, K. Z.; Zhao, Y.; Jiao, L. F.; Wang, Y. J.; Yuan, H. T. Update on anode materials for Na-ion batteries. *J. Mater. Chem. A* **2015**, *3*, 17899–17913.

[40] Park, G. D.; Cho, J. S.; Kang, Y. C. Sodium-ion storage properties of nickel sulfide hollow nanospheres/reduced graphene oxide composite powders prepared by a spray drying process and the nanoscale kirkendall effect. *Nanoscale* **2015**, *7*, 16781–16788.

[41] Wang, T. S.; Hu, P.; Zhang, C. J.; Du, H. P.; Zhang, Z. H.; Wang, X. G.; Chen, S. G.; Xiong, J. W.; Cui, G. L. Nickel disulfide-graphene nanosheets composites with improved electrochemical performance for sodium ion battery. *ACS Appl. Mater. Interfaces* **2016**, *8*, 7811–7817.

[42] Sun, Y. M.; Hu, X. L.; Luo, W.; Xia, F. F.; Huang, Y. H. Reconstruction of conformal nanoscale MnO on graphene as a high-capacity and long-life anode material for lithium ion batteries. *Adv. Funct. Mater.* **2013**, *23*, 2436–2444.

[43] Lee, S. M.; Choi, S. H.; Kang, Y. C. Electrochemical properties of tin oxide flake/reduced graphene oxide/carbon composite powders as anode materials for lithium-ion batteries. *Chem.—Eur. J.* **2014**, *20*, 15203–15207.

[44] Li, N.; Liu, G.; Zhen, C.; Li, F.; Zhang, L. L.; Cheng, H. M. Battery performance and photocatalytic activity of mesoporous anatase TiO_2 nanospheres/graphene composites by template-free self-assembly. *Adv. Funct. Mater.* **2011**, *21*, 1717–1722.